DOI: 10.19884/j.1672-5220.202511003

Feature-Based Precise Identification of Point Clouds in Weld Regions

MA Da[1], PANG Shaoru[1], WANG Qingxia[1,3*], WU Chongjun[1], DONG Jiyi[2,3]
1. School of Mechanical Engineering, Donghua University, Shanghai 201620, China
2. Shanghai Aerospace Equipment Manufacturer Co., Ltd., Shanghai 200245, China
3. Shanghai Aerospace Process and Equipment Engineering and Technology Research Center, Shanghai 200245, China

Abstract: To enhance the accuracy of weld region identification under structured light vision guidance while maintaining method robustness, this paper proposes an adaptive weld identification method fusing local morphological and spatial position features. First, a fused feature space for point cloud data is constructed based on curvature estimation and spatial distance calculation, and the Gaussian mixture model (GMM) is adopted for unsupervised iterative learning of point cloud data to realize the extraction of feature points in the weld region. Second, combining with the hierarchical density-based spatial clustering of applications with noise (HDBSCAN) and voxel connectivity block analysis, the precise segmentation and boundary refinement optimization of the weld region are completed. Finally, experimental results demonstrate that this method achieves a precision of 99.38%, a recall of 88.41%, and an F1 score of 93.57% in identifying V-groove regions in circumferential welds, outperforming comparison methods such as random sample consensus combined with density-based spatial clustering of applications with noise (RANSAC-DBSCAN). Furthermore, the boundary localization error is less than 0.3 mm; parameter tests verify that the proposed method has low parameter sensitivity and strong stability, which meets practical production requirements.

Keywords: structured light; point cloud data; weld region identification; Gaussian mixture model; hierarchical density clustering
CLC number: TP274+.5 **Document code**: A
Article ID: 1672-5220(2026)04-0119-14

0 Introduction

In high-end manufacturing fields such as automotive pressure vessels, marine pressure hulls, and rocket launch containers, the weld region serves as the core area for structural connection and force transmission. The geometric precision and surface quality of these regions directly determine the sealing integrity, structural strength, and service life of the equipment[1]. In recent years, the integration of machine vision technology into robotic welding systems has enabled welding robots to autonomously identify weld regions and geometric features in real time by using visual sensing. This facilitates dynamic path planning for batch-welding operations[2-3]. Consequently, stringent requirements now exist for pre-machining dimensions, assembly accuracy, weld start-point guidance[4], and positioning accuracy during welding. In summary, achieving precise extraction and tracking control of the weld geometry during welding is crucial for ensuring weld quality and represents an urgent engineering challenge to be resolved.

In practical industrial scenarios, butt-weld regions exhibit varying assembly states, and metallic materials possess high reflectivity[5]. Additionally, the weld region and its connecting area often share similar geometric features with the base material, making it difficult to clearly define the region boundary. With the advancement of three-dimensional (3D) vision technology, 3D reconstruction methods using point clouds have provided new approaches for region identification, which can accurately acquire the 3D structural information of workpieces and are less affected by environmental factors such as lighting[6-7].

Existing weld identification methods using point clouds can be categorized into three types. The first type is based on single geometric features. Early studies primarily relied on local geometric features such as curvature and normal vectors for region segmentation. Qian et al.[8] proposed an improved boundary-tracking weld identification method, using curvature angle estimation to determine weld regions. Ma et al.[9] extracted point cloud surface features through an enhanced normal vector estimation method, and segmented target regions based on normal vector direction consistency. Although these methods are computationally simple, their discriminative ability is limited under conditions of small feature differences or noise interference, which easily leads to incorrect feature extraction. The second type is based on multi-feature fusion and geometric model fitting. To enhance recognition robustness, some studies have shifted toward strategies integrating multiple features

Received date: 2025-11-09
* Correspondence should be addressed to WANG Qingxia, email: wqxia@dhu.edu.cn
Citation: Ma D, Pang S R, Wang Q X, et al. Feature-based precise identification of point clouds in weld regions[J]. *Journal of Donghua University (English Edition)*, 2026, 43(4): 119-132.

and geometric model fitting. Yang et al.[10] proposed fitting workpiece planes using random sample consensus (RANSAC), then utilizing point-to-plane distance features to segment lines and surfaces, thereby identifying the weld region. Zhang et al.[11] performed preliminary classification based on the point cloud plane density, followed by locating feature regions through line fitting and centroid position. Although these methods enhance feature representation to some extent, their inherent reliance on geometric model fitting limits their adaptability when encountering complex structures or assembly deviations. The third type is based on feature similarity clustering. To improve adaptability to complex structures, researchers have introduced clustering or region-growing algorithms based on feature similarity. Gao et al.[12] used normals and curvature as similarity criteria to progressively merge point clouds with consistent features within a neighborhood, achieving a weld region of interest (ROI) extraction. Zhang et al.[13] employed density-based spatial clustering of applications with noise (DBSCAN) to segment blade point clouds, identifying weld region feature points through concavity descriptors and K-means clustering. Zheng et al.[14] addressed surface crack defects in steel. They first segmented the steel plane using the RANSAC algorithm, and then applied DBSCAN to the segmented point cloud for defect region localization. In the work of Ke et al.[15], even after successful non-rigid registration between shoe soles and uppers, trajectory segmentation still relied on traditional clustering methods, which required manual parameter tuning during the end point recognition stage. Although such methods demonstrate improved adaptability to complex structures, region-growing algorithms are inherently dependent on the selection of initial seed points and the setting of similarity thresholds. Since parameter calibration is heavily reliant on manual experience, these methods suffer from limited generalization capability, which severely restricts their practical deployment in variable industrial scenarios.

In summary, existing methods in complex industrial scenarios suffer from issues such as reliance on single or fixed feature combinations, insufficient robustness to noise and local geometric changes, difficulty in adapting to complex working conditions, parameter sensitivity, and lack of adaptive capabilities. Therefore, this paper proposes an adaptive circumferential weld region identification algorithm fusing local and spatial features. Taking simulated point clouds of weld regions in pressure vessels as the research object, the method aims to achieve weld region identification with high precision, high robustness, and real-time performance requirements under structured light vision guidance. By exploiting the complementarity between local curvature features and spatial distance features, combined with the adaptive discriminative capability of the Gaussian mixture model (GMM) in fused feature space and the technical advantage of hierarchical density-based spatial clustering of applications with noise (HDBSCAN) in handling non-uniform density point cloud clustering, the method is expected to provide 3D data of the target region for subsequent dimensional measurement, defect detection, and welding path planning.

1 Weld Region Identification Process

Under structured light vision guidance, the sensor is mounted at the front end of the welding gun to scan the circumferential weld region. Through the trajectory recognition process, the sensor acquires the weld region points and transmits the data to the motion control model, thereby executing a series of intelligent welding operations. Therefore, the precise identification of the circumferential weld region is critical for achieving successful welding.

Weld characteristics primarily encompass the joint configuration and groove type. This study focuses on the circumferential weld region with predominantly V-groove configurations, as illustrated in Figs. 1(a) and 1(b). h denotes the height of the butt-weld region, θ_1 represents the angle between vectors $\overrightarrow{A_1B_1}$ and $\overrightarrow{B_1C_1}$, and θ_2 denotes the angle between vectors $\overrightarrow{A_2B_2}$ and $\overrightarrow{B_2C_2}$. Under ideal conditions, the V-groove B_1A_1 and B_2A_2 aligns perfectly, meaning the butt-weld assembly gap $l_1 = 0$. l_2 represents the actual width of the V-groove.

Although structured light vision equipment typically captures the circumferential weld region that shows distinct geometric or morphological changes relative to the surrounding base material surface, as illustrated in Fig. 1(c), workpiece assembly gap deviation Δ_1 and Δ_2 arise during the assembly process, and manufacturing dimension error Δ_3 occurs during the welding process. These deviations can lead to discrepancies between spatial dimensions, such as the weld width and depth, and their actual specifications. The misalignment caused by Δ_1 alters the alignment angle of the groove, while the gap fluctuation from Δ_2 affects the opening width of the groove. These deviations may result in varying orientations of the V-groove, which could exceed the allowable range of the welding process. In addition, existing weld region identification methods often suffer from over-extraction or under-extraction issues due to factors like reflections, camera blind spots and gradual shape transitions. These factors collectively increase the complexity of weld region identification.

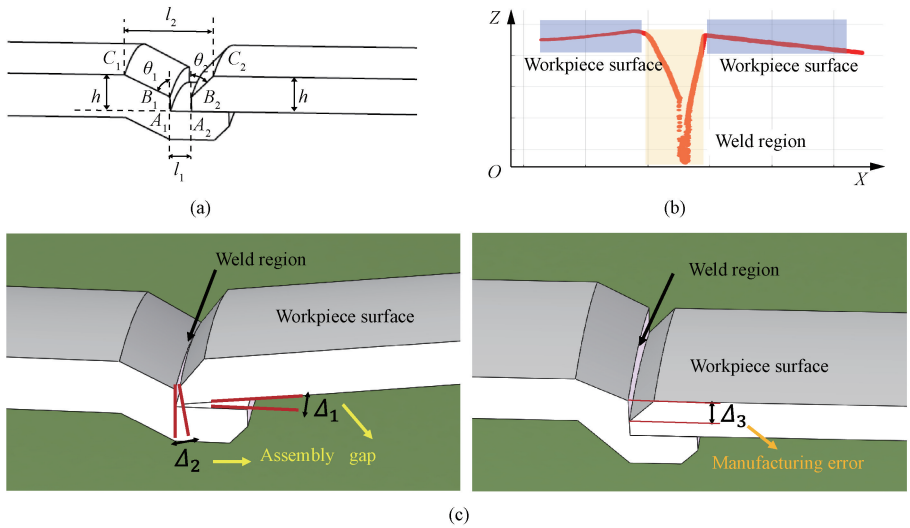


Fig. 1 Circumferential weld region: (a) V-groove configurations; (b) weld section point cloud; (c) simulated V-groove orientation

In this study, high-precision extraction of the circumferential weld region is achieved through unsupervised learning by exploiting the complementarity between local curvature features and spatial distance features. The algorithmic workflow is illustrated in Fig. 2.

1) Point cloud data acquisition and preprocessing. Preprocess the raw point cloud to enhance subsequent processing efficiency. First, pass-through filtering is employed to remove background and non-target point clouds in the sensor field of view, retaining only the circumferential weld region and adjacent base material point clouds. Second, voxel grid down-sampling is performed. The point cloud space is divided into uniform voxel grids, and the centroid of the point cloud within each voxel is used as the representative point. In this study, the voxel side length is set to 0.2 mm. This parameter maintains the geometric features of the circumferential weld region while enhancing the computational efficiency of subsequent feature extraction and clustering.

2) Extraction of feature points. The point cloud curvature is estimated and a base material reference plane is fitted. The distance from each point to the fitted plane is calculated. A fused feature space is constructed based on local curvature estimation and spatial distance calculation, which enables the automatic extraction of characteristic points in the suspected circumferential weld region by using a GMM.

3) Weld point cloud clustering. Feature points are adaptively clustered through HDBSCAN, and voxel grid connected component is combined to achieve precise weld region identification.

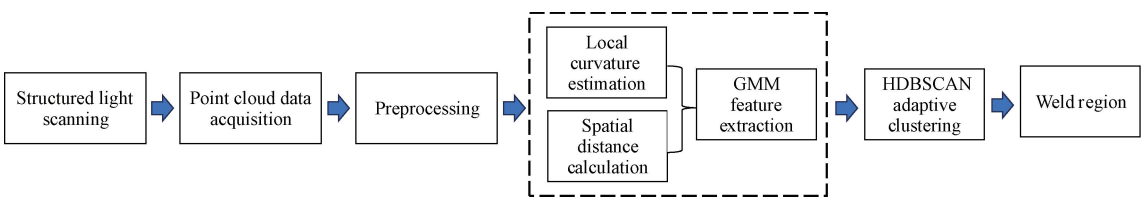


Fig. 2 Flowchart of proposed algorithm

2 Extraction of Feature Points

Effective feature extraction from point cloud data is essential for achieving automatic weld region identification. This study first calculates the curvature features reflecting surface morphology changes and distance features reflecting the spatial relationship between the point cloud and the base material reference plane based on the local geometric properties of the point cloud. These multidimensional features are then fused and extracted using a GMM.

2.1 Local curvature estimation

The normal vectors of the preprocessed point cloud are estimated using the principal component analysis (PCA). For each point $\boldsymbol{p}_i = (x_i, y_i, z_i)$, where x_i, y_i and z_i are the coordinates of the point $\boldsymbol{p}_i$ in 3D space, $i = 1, 2, \cdots, K$, and K denotes the number of neighborhood points. The K-nearest neighbor (KNN) method is used to determine the local neighborhood. The centroid $\bar{\boldsymbol{q}}$ of its neighborhood points is

$$\bar{\boldsymbol{q}} = \frac{1}{K}\sum_{i=1}^{K}\boldsymbol{p}_i. \tag{1}$$

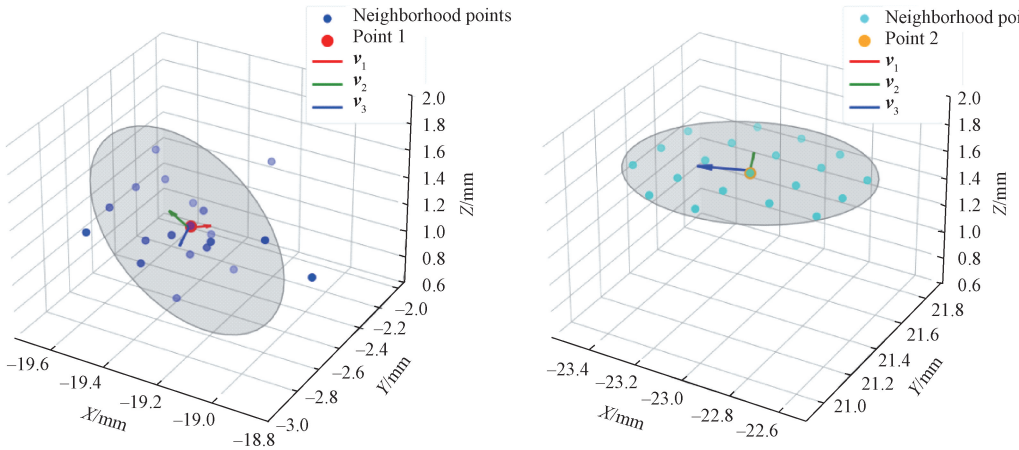
Construct the covariance matrix $\boldsymbol{C}_i$ of the neighborhood points around the centroid $\bar{\boldsymbol{q}}$:

$$\boldsymbol{C}_i = \frac{1}{K}\sum_{i=1}^{K}(\boldsymbol{p}_i - \bar{\boldsymbol{q}})(\boldsymbol{p}_i - \bar{\boldsymbol{q}})^{\mathrm{T}}, \tag{2}$$

where $\boldsymbol{p}_i - \bar{\boldsymbol{q}}$ represents the deviation vector of each point $\boldsymbol{p}_i$ from the centroid $\bar{\boldsymbol{q}}$. This vector quantifies the displacement of each point relative to the centroid in 3D space.

Eigenvalue decomposition of the covariance matrix $\boldsymbol{C}_i$ yields three eigenvalues λ_1, λ_2 and λ_3 (ordered as $\lambda_1 \leqslant \lambda_2 \leqslant \lambda_3$) with corresponding eigenvectors $\boldsymbol{v}_1$, $\boldsymbol{v}_2$ and $\boldsymbol{v}_3$.

Arbitrary points are selected within both the weld region and the base material region. The domain point distributions and the eigenvalues of the covariance matrix are shown in Fig. 3. For the same number of neighborhood points, the dispersion of points in the weld region relative to the fitted surface is greater than that in the base material region. The eigenvector $\boldsymbol{v}_1$ corresponding to the minimum eigenvalue λ_1 represents the normal vector, where the magnitude of the normal vector for the weld region is significantly higher than that for the base material region. Thus, the minimum eigenvalue λ_1 reflects the undulation of the point cloud along the normal vector direction. Consequently, this study employs the normal vector at each point for local curvature estimation.



(a) (b)

Fig. 3 Neighborhood points and eigenvectors of an arbitrary point in point cloud: (a) arbitrary point in weld region; (b) arbitrary point in base material region

To quantify the local curvature of a point cloud surface, the ratio of the lowest eigenvalue to the sum of all eigenvalues is commonly used. This ratio is defined as

$$c_i = \frac{\min\{\lambda_1, \lambda_2, \lambda_3\}}{\lambda_1 + \lambda_2 + \lambda_3}, \tag{3}$$

where c_i represents the curvature at point $\boldsymbol{p}_i$, which indicates the degree of local surface undulation in the weld region compared to the base material surface.

Figure 4 illustrates the curvature feature distribution of point clouds. The curvature values in the weld region generally exceed those in the base material region. In addition, both regions exhibit point cloud distributions with identical curvature values. For instance, a distribution range of 0.001 and 0.002 may result from factors such as small chamfer dimensions at connections or large butt gaps. Furthermore, areas with anomalous curvature values exhibit random characteristics, which can be regarded as noise points in the point cloud. These anomalies may stem from measurement errors of the instrument or surface defects such as holes in the weld region.

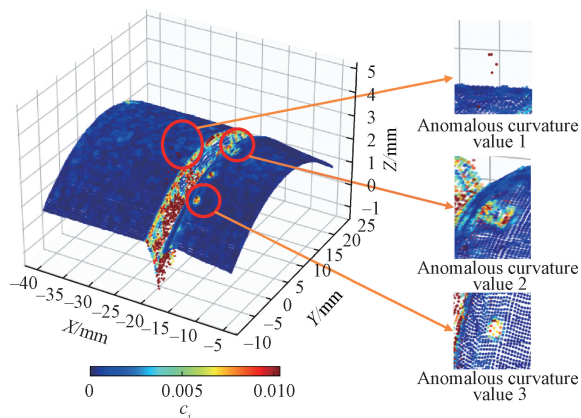


Fig. 4 Distribution of curvature features

2.2 Spatial distance calculation

The existence of a spatial distance between the weld region and the workpiece surface is a physical fact[16]. To enhance feature recognition capability, this study further introduces the distance from the point cloud to the fitted base material reference plane as a recognition feature. Specifically, the surface of a cylindrical workpiece is selected as the reference plane, and the spatial distance from each point to this reference plane is calculated.

Generalized quadratic surface fitting is used to describe mathematical models of noisy point cloud object surfaces[17].

Let any quadratic surface equation be

$$\boldsymbol{x}^{\mathrm{T}}\boldsymbol{A}\boldsymbol{x} + \boldsymbol{b}^{\mathrm{T}}\boldsymbol{x} + \boldsymbol{k} = 0, \tag{4}$$

where $\boldsymbol{x} = [x \quad y \quad z]^{\mathrm{T}}$ is the spatial point coordinate; $\boldsymbol{A} \in \mathbf{R}^{3\times3}$ is a symmetric matrix; $\boldsymbol{b} \in \mathbf{R}^{3}$ is a vector; $\boldsymbol{k} \in \mathbf{R}$ is a scalar.

For a point cloud $\{\boldsymbol{x}_i = [x_i \quad y_i \quad z_i]^{\mathrm{T}}\}_{i=1}^{N}$ consisting of N points, the fitting objective is to find a set of parameters $\{\boldsymbol{A}, \boldsymbol{b}, \boldsymbol{k}\}$ that minimizes the sum of squared algebraic residuals for all points and the cost function E^2:

$$E^2 = \frac{1}{N}\sum_{i=1}^{N}(\boldsymbol{x}_i^{T}\boldsymbol{A}\boldsymbol{x}_i + \boldsymbol{b}^{\mathrm{T}}\boldsymbol{x}_i + \boldsymbol{k})^2. \tag{5}$$

Construct the second-order moment matrix $\boldsymbol{M}$ and the constraint matrix $\boldsymbol{O}$ to solve the generalized eigenvalue problem:

$$\boldsymbol{M}\theta = \eta\boldsymbol{O}\theta, \tag{6}$$

where $\boldsymbol{\theta} = [\mathrm{vec}(\boldsymbol{A})^{\mathrm{T}} \quad \boldsymbol{b}^{\mathrm{T}} \quad \boldsymbol{k}]^{\mathrm{T}}$ is the vector of surface parameters; η denotes the generalized eigenvalue. The eigenvector corresponding to the lowest eigenvalue η^* represents the optimal parameters $\boldsymbol{\theta}^* = [\mathrm{vec}(\boldsymbol{A}^*)^{\mathrm{T}} \quad (\boldsymbol{b}^*)^{\mathrm{T}} \quad \boldsymbol{k}^*]^{\mathrm{T}}$, where $\boldsymbol{A}^*$, $\boldsymbol{b}^*$, $\boldsymbol{k}^*$ denote the converged final values of $\{\boldsymbol{A}, \boldsymbol{b}, \boldsymbol{k}\}$ obtained after solving the generalized eigenvalue problem, which are used to reconstruct the fitted reference surface.

$$f(x) = \boldsymbol{x}^{\mathrm{T}}\boldsymbol{A}^*\boldsymbol{x} + (\boldsymbol{b}^*)^{\mathrm{T}}\boldsymbol{x} + \boldsymbol{k}^*. \tag{7}$$

The approximate spatial distance d_i between any point $\boldsymbol{x}_i$ in the point cloud and the fitted surface can be estimated by the ratio of its algebraic residual to the gradient magnitude:

$$d_i = \frac{|f(\boldsymbol{x}_i)|}{|\nabla f(\boldsymbol{x}_i)|} = \frac{|\boldsymbol{x}_i^{\mathrm{T}}\boldsymbol{A}^*\boldsymbol{x}_i + (\boldsymbol{b}^*)^{\mathrm{T}}\boldsymbol{x}_i + \boldsymbol{k}^*|}{|\nabla f(\boldsymbol{x}_i)|}. \tag{8}$$

This distance metric quantifies the spatial deviation of each point relative to the fitted reference surface of the base material. As shown in Fig. 5(a), the fitted reference surface obtained via generalized quadratic surface fitting exhibits low sensitivity to noise and closely conforms to the base material point cloud surface. Furthermore, the distance feature distribution in Fig. 5(b) reveals higher distance values in the weld region and lower values in the base material region, confirming the effectiveness of this feature in distinguishing between these two regions.

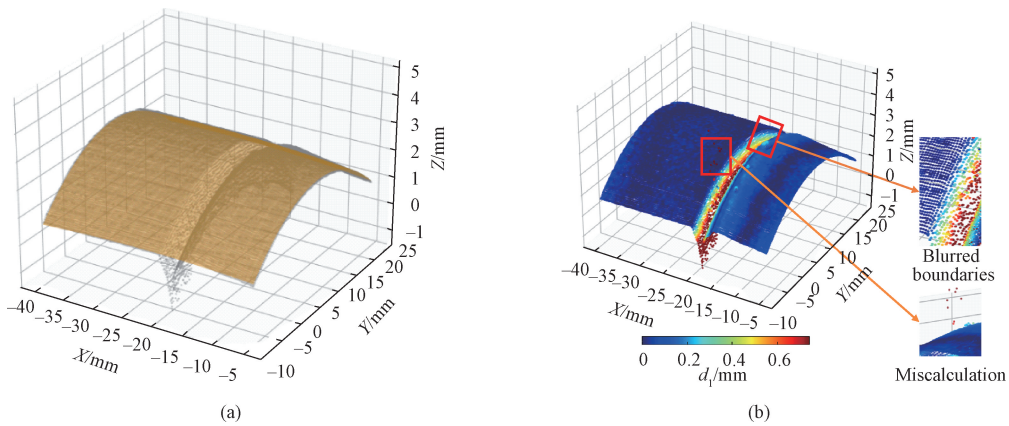


Fig. 5 Fitted surface and feature distribution: (a) fitted surface; (b) point-to-surface distance feature distribution

However, the distance from the edge of the weld region to the reference surface shows no significant difference from that in the base material region, leading to blurred boundary resolution. Furthermore, isolated noise points generate anomalous distance responses in d_i, forming spurious features. Therefore, this study fuses the distance and curvature features to construct a more discriminative feature space.

2.3 GMM-based weld feature point extraction

As a generative probabilistic model, the GMM can learn the intrinsic substructures of data under unsupervised conditions using the expectation-maximization (EM) algorithm, enabling soft segmentation of samples based on posterior probabilities.

Let the feature vector of each point cloud sample be $\boldsymbol{f}_i = [c_i \quad d_i]^{\mathrm{T}}$. Since there are significant differences in dimensions and value ranges between c_i and d_i, directly concatenating them into a two-dimensional (2D) feature vector may cause one feature to dominate the GMM, affecting the effective fusion of the two features. To balance the feature weights, this study adopts the Z-score standardization method to normalize the two types of features.

$$c_i^* = \frac{c_i - \mu_{\mathrm{c}}}{\sigma_{\mathrm{c}}}, \quad d_i^* = \frac{d_i - \mu_{\mathrm{d}}}{\sigma_{\mathrm{d}}}, \tag{9}$$

where μ_{c} and σ_{c} are the mean and standard deviation of the curvature feature, respectively; μ_{d} and σ_{d} are the mean and standard deviation of the distance feature, respectively; c_i^* and d_i^* are the normalized feature values.

The normalized feature vector is $\boldsymbol{f}_i^* = [\, c_i^* \;\; d_i^* \,]^{\mathrm{T}}$.

The purpose of feature extraction is to initially segment the point cloud into weld regions and non-weld regions, which is essentially a binary classification problem. Therefore, based on the prior information of the problem, GMM is selected as the adaptive classifier, and the number of Gaussian components G is set to 2, corresponding to the two potential Gaussian distributions of weld and non-weld.

The normalized fused feature samples $\boldsymbol{f}_i^*$ are input into the GMM model. Based on the binary classification setting, the combined distribution of all samples can be approximated as a weighted sum of two 2D Gaussian distributions, and its probability density function is

$$F(\boldsymbol{f}_i^*) = \sum_{g=1}^{G} \pi_g \cdot N(\boldsymbol{f}_i^* \mid \boldsymbol{\nu}_g, \boldsymbol{\Sigma}_g), \tag{10}$$

where π_g is the mixing coefficient for the gth Gaussian distribution, satisfying $\sum_{g=1}^{G} \pi_g = 1$; $N(\boldsymbol{f}_i^* \mid \boldsymbol{\nu}_g, \boldsymbol{\Sigma}_g)$ is the probability density function of a Gaussian distribution with a mean of $\boldsymbol{\nu}_g$ and a covariance $\boldsymbol{\Sigma}_g$, expressed as

$$N(\boldsymbol{f}_i^* \mid \boldsymbol{\nu}_g, \boldsymbol{\Sigma}_g) = \frac{1}{2\pi \mid \boldsymbol{\Sigma}_g \mid^{1/2}} \exp\left[-\frac{1}{2} (\boldsymbol{f}_i^* - \boldsymbol{\nu}_g)^{\mathrm{T}} \boldsymbol{\Sigma}_g^{-1} (\boldsymbol{f}_i^* - \boldsymbol{\nu}_g) \right]. \tag{11}$$

In this method, the two components of $\boldsymbol{f}_i^*$ correspond to the curvature and distance to the fitted reference surface of the point cloud. Therefore, the feature space dimension is 2. The GMM parameters $\Omega = \{\pi_1, \pi_2, \boldsymbol{\nu}_1, \boldsymbol{\nu}_2, \boldsymbol{\Sigma}_1, \boldsymbol{\Sigma}_2\}$ are estimated using the EM algorithm. For each sample point $\boldsymbol{f}_i^*$, the posterior probability belonging to each Gaussian distribution is calculated as

$$\gamma_{ig}^{(t)} = F(g \mid \boldsymbol{f}_i^*, \Omega^{(t)}) = \frac{\pi_g^{(t)} N(\boldsymbol{f}_i^* \mid \boldsymbol{\nu}_g^{(t)}, \boldsymbol{\Sigma}_g^{(t)})}{\sum_{g=1}^{G} \pi_g^{(t)} N(\boldsymbol{f}_i^* \mid \boldsymbol{\nu}_g^{(t)}, \boldsymbol{\Sigma}_g^{(t)})}, \tag{12}$$

where t denotes the current iteration step of the EM algorithm; $\Omega^{(t)}$, $\gamma_{ig}^{(t)}$, $\pi_g^{(t)}$, $\boldsymbol{\nu}_g^{(t)}$ and $\boldsymbol{\Sigma}_g^{(t)}$ represent their parameter values at the current iteration step t. $\Omega^{(t)}$ represents the set of all GMM parameters at iteration t; $\gamma_{ig}^{(t)}$ is the posterior probability that the ith sample belongs to the gth Gaussian component; $\pi_g^{(t)}$, $\boldsymbol{\nu}_g^{(t)}$ and $\boldsymbol{\Sigma}_g^{(t)}$ are the mixing coefficient, mean vector, and covariance matrix of the gth component; $N(\boldsymbol{f}_i^* \mid \boldsymbol{\nu}_g^{(t)}, \boldsymbol{\Sigma}_g^{(t)})$ denotes the multivariate Gaussian distribution with mean $\boldsymbol{\nu}_g^{(t)}$ and covariance $\boldsymbol{\Sigma}_g^{(t)}$.

All Gaussian components must be traversed to compute the joint contribution probability of all Gaussian components to the current sample through summation. The EM algorithm iteratively optimizes to gradually approximate the optimal parameters until convergence conditions are satisfied.

Based on the posterior probability $\gamma_{ig}^{(t)}$ at the current iteration step t, the mixing coefficient, mean vector, and covariance matrix are updated as follows.

$$\pi_g^{(t+1)} = \frac{1}{N} \sum_{i=1}^{N} \gamma_{ig}^{(t)}, \tag{13}$$

$$\boldsymbol{\nu}_g^{(t+1)} = \frac{\sum_{i=1}^{N} \gamma_{ig}^{(t)} \boldsymbol{f}_i^*}{\sum_{i=1}^{N} \gamma_{ig}^{(t)}}, \tag{14}$$

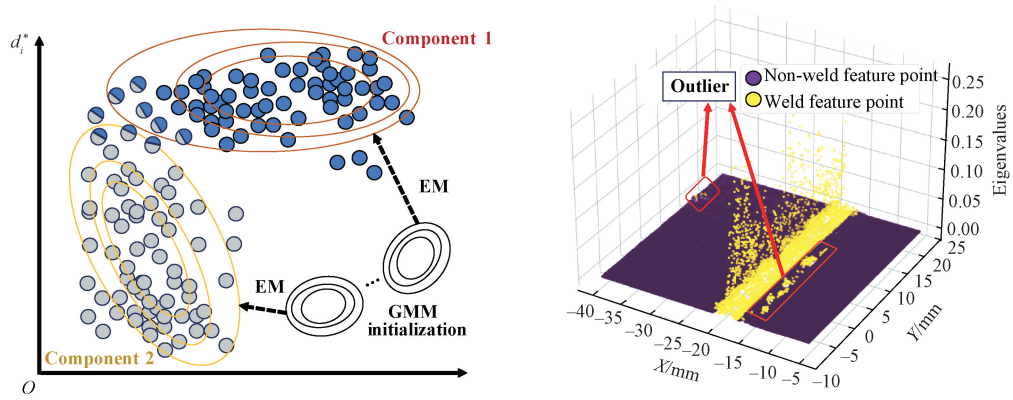
$$\boldsymbol{\Sigma}_g^{(t+1)} = \frac{\sum_{i=1}^{N} \gamma_{ig}^{(t)} (\boldsymbol{f}_i^* - \boldsymbol{\nu}_{ig}^{(t)}) (\boldsymbol{f}_i^* - \boldsymbol{\nu}_{ig}^{(t)})^{\mathrm{T}}}{\sum_{i=1}^{N} \gamma_{ig}^{(t)}}, \tag{15}$$

where N is the total number of samples. Repeat the above EM iteration process, and compute the log-likelihood function for each EM iteration:

$$\ln L(\Omega^{(t+1)}) = \sum_{1}^{N} \ln(\pi_g^{(t+1)} N(\boldsymbol{f}_i^* \mid \boldsymbol{\nu}_g^{(t+1)}, \boldsymbol{\Sigma}_g^{(t+1)})). \tag{16}$$

When the change in log-likelihood between two adjacent iterations converges, the EM algorithm stops and obtains the final GMM parameters $\Omega^* = \{\pi_1^*, \pi_2^*, \boldsymbol{\nu}_1^*, \boldsymbol{\nu}_2^*, \boldsymbol{\Sigma}_1^*, \boldsymbol{\Sigma}_2^*\}$ under the given condition $G = 2$.

Figure 6(a) shows the different components that represent the two Gaussian components obtained through the EM algorithm, and the dashed arrows reflect the dynamic optimization process of the Gaussian components from the initial state to the final convergence during the EM iteration. Based on the final GMM, each $\boldsymbol{f}_i^*$ is assigned to the Gaussian distribution with the highest probability according to its posterior probability, and the two Gaussian distributions correspond to the weld and non-weld feature points, respectively. The feature point extraction results are shown in Fig. 6(b). This process automatically models the feature extraction through unsupervised learning without setting classification thresholds, realizing the adaptive extraction of weld region feature points. However, the weld region feature points processed by the GMM still contain noise and outliers.



(a) (b)

Fig. 6 Feature extraction and visualization results based on GMM: (a) component evolution and point assignment during EM iteration; (b) feature point extraction results

3 Weld Region Point Cloud Clustering

After feature point extraction using the GMM, the feature point set has initially distinguished the weld regions from the base material. However, the results still contain two types of interfering point sets: low-density and spatially discrete outliers, and points with sufficient density but spatially separated from the weld region. Clustering methods based on feature similarity, such as K-means and spectral clustering, have already considered relevant features during feature extraction and ignore the 3D spatial distribution characteristics, making it impossible to further improve the discriminative ability. Weld regions should exhibit spatially continuous and uniformly dense entities in the physical space. To utilize the spatial information of feature points, a density-based clustering strategy is selected in this study.

As shown in Fig. 6, the feature points in the weld region exhibit a highly cohesive distribution in the normalized fused feature space. This means that the region maintains high point set integrity under different density thresholds, demonstrating strong robustness to variations in density thresholds. Traditional density-based clustering methods rely on preset global density parameters. Using fixed thresholds for clustering not only makes parameter selection difficult but also loses adaptability to density changes. In contrast, if iterative screening is performed using hierarchical density parameters, the weld region will continuously exhibit the most stable main cluster across multiple threshold levels. Therefore, this study adopts the HDBSCAN algorithm to extract the most stable main cluster based on cluster stability metrics at different densities. The specific steps include density estimation, minimum spanning tree (MST) construction, hierarchical structure construction, stable cluster extraction and voxel grid connected component analysis.

3.1 Density estimation

For each feature point p'_i, calculate its core distance $d_c(p'_i)$ to estimate the density of its surrounding region:

$$d_c(p'_i) = \min\{r \mid p'_j \mid \{d(p'_i,p'_j) \leqslant r \mid \geqslant \tau\}\}, \quad (17)$$

where τ denotes the minimum number of points within a cluster, which is the only parameter of HDBSCAN; r represents the minimum radius of a sphere centered at the point p'_i that contains at least τ points; p'_j indicates the nth nearest neighborhood points of p'_i; $d(p'_i, p'_j)$ denotes the Euclidean distance between two points. τ is based on a prior estimation of the size of typical outlier sets, aiming to filter small-scale pseudo-clusters formed by local outliers or isolated points. In this study, it is set to 1% of the total input point cloud.

3.2 MST construction

To better characterize the significant difference between the noise points and weld region points, we introduced the reachability distance d_m:

$$d_m(p'_i, p'_j) = \max\{d_c(p'_i), d_c(p'_j), d(p'_i, p'_j)\}. \quad (18)$$

The reachability distance between all point pairs is used to construct a weighted undirected graph $U = (R, W)$, where R is the vertex set, containing all feature points to be clustered; W is the edge set, comprised of the connection relationships between all feature point pairs.

The weight $w(p'_i, p'_j)$ of each edge $(p'_i, p'_j) \in W$ is defined as the reachability distance between the corresponding point pair:

$$w(p'_i, p'_j) = d_m(p'_i, p'_j). \quad (19)$$

The MST, denoted as T, is the minimum connected subgraph of all nodes, and its construction must satisfy two core conditions: it includes all vertices of U; it uses the minimum number of edges to achieve connectivity of all vertices with the minimum total edge weight. Since both the vertices and edges of T are derived from U, T is a subgraph of U. The expression of T constructed based on the reachability distance is

$$T = \arg\min_{T \subseteq U} \sum_{(p'_i, p'_j) \subseteq W_T} w(p'_i, p'_j), \quad (20)$$

where W_T denotes the edge subset within T.

3.3 Hierarchical structure construction

First, a density threshold φ, which is inversely proportional to the density, is defined. For a given φ, all

edges in T with weights $w(p'_i, p'_j)$ exceeding the threshold φ are removed. The remaining connected components $\{L_\varphi\}$ constitute the clustering result at this threshold. By iteratively decreasing the density threshold φ from its initial maximum value φ_{max} down to $\varphi = 0$, all edges are eventually removed. Each node is then connected to form a single entity, generating a hierarchical clustering tree H as shown in Fig. 7(a). This hierarchical clustering tree H can be represented as the cluster partition resulting from the iteration:

$$H = \{L_{\varphi,l} \mid \varphi \in [0, \varphi_{max}]\}, \tag{21}$$

where l represents the number of clusters in the cluster partitioning result; $L_{\varphi,l}$ denotes the lth cluster at a density threshold of φ.

3.4 Stable cluster extraction

The stability of a cluster is comprehensively reflected by the integral of the cluster over the density threshold sequence:

$$S(L_{\varphi,l}) \approx \int_{\lambda_\alpha}^{\lambda_\beta} |L_{\varphi,l}| \, d\varphi, \tag{22}$$

where λ_β and λ_α denote the density thresholds at which a cluster $L_{\varphi,l}$ appears or merges into a larger cluster; $|L_{\varphi,l}|$ is the number of sample points contained in the lth cluster at the density threshold.

Figure 7(b) illustrates the distribution of clusters in 3D space after HDBSCAN clustering. Different colors represent distinct clusters. The weld region is effectively clustered into the main cluster, whereas the misclassified feature points form smaller clusters. The noise points and edge anomalies are clearly separated.

3.5 Voxel grid connected component analysis

To maintain the spatial continuity of the weld region point cloud and improve the boundary accuracy, spatial connectivity constraints are introduced based on HDBSCAN. Micro point sets that meet clustering conditions but are spatially discrete from the weld region are eliminated through voxel grid connected component analysis.

As shown in Fig. 7(c), the main cluster point set is mapped onto the voxel grid. The centroid of the non-empty point set within each voxel is computed as the representative point. For each representative point, a connected component analysis is performed within a defined search radius based on the 26-neighborhood. The 26-neighborhood refers to the full set of adjacent voxels surrounding a target voxel in 3D space, covering 6 face-adjacent, 12 edge-adjacent and 8 corner-adjacent voxels. If there exists at least one other non-empty voxel within the neighborhood of this point, and any voxel contains at least as many points as the minimum cluster size in HDBSCAN, then this voxel is marked as a connected point. If other extracted points within the neighborhood satisfy the minimum point threshold, the voxel is marked as being connected. Otherwise, it is marked as isolated. Through this connectivity determination, high-density connected regions are formed via region growing.

Figure 7(d) shows the results after the connected component post-processing. The noise points attached to the edges of the main cluster were effectively removed. The boundaries of the weld regions were clearer and more regular than the initial cluster results, accurately reflecting the actual physical contours of the weld regions.

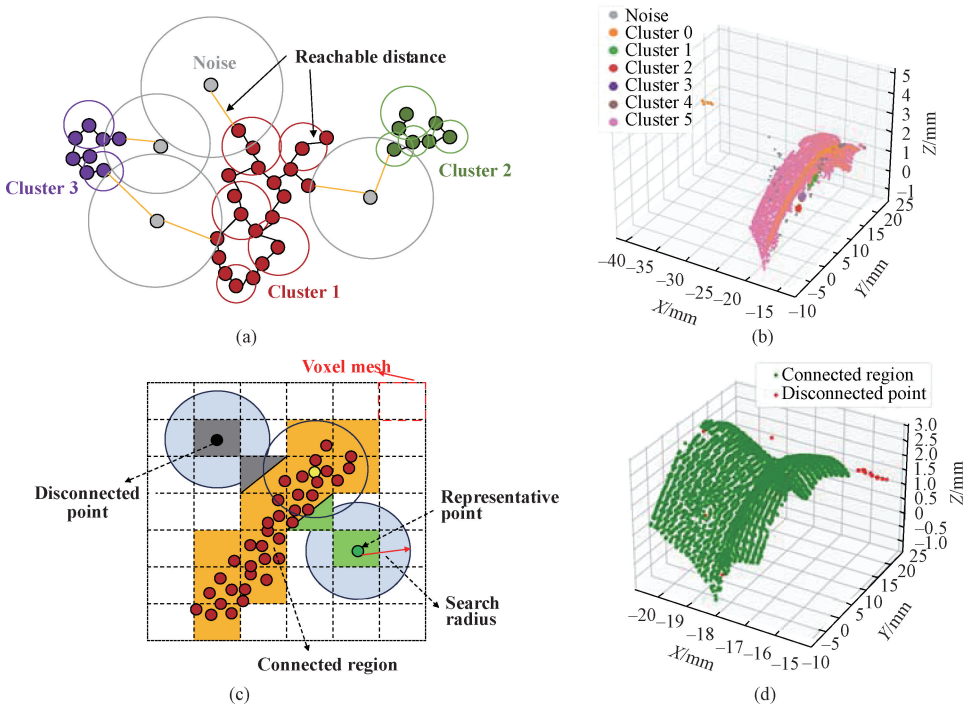


Fig. 7 Precise segmentation of point clouds: (a) hierarchical clustering tree; (b) HDBSCAN cluster results; (c) voxel connected component analysis; (d) precise cluster results

4 Experiment and Evaluation Metrics

To validate the effectiveness of the proposed GMM-HDBSCAN method in engineering practice, weld region images were collected on-site from the production facility of an air suspension tank at a company, as shown in Fig. 8. Precision P, recall R, F1 score F_1, relative error V_{RE}, and algorithm runtime are adopted as core evaluation metrics:

$$\begin{cases} P = \dfrac{V_{TP}}{V_{TP} + V_{FP}}, \\ R = \dfrac{V_{TP}}{V_{TP} + V_{FN}}, \\ F_1 = 2 \times \dfrac{P \times R}{P + R}, \\ V_{RE} = \dfrac{|n - n'|}{n} \times 100\%, \end{cases} \tag{23}$$

where n and n' represent the number of points in the weld region point cloud and the number of feature points extracted by the proposed algorithm; true positive V_{TP}, false positive V_{FP}, and false negative V_{FN} denote the number of correctly identified weld region point clouds, false positive point clouds, and false negative point clouds, respectively.

To evaluate the proposed algorithm, comparative experiments were conducted using multiple weld region identification methods, including single-feature methods, feature fusion with different clustering methods, and other types of methods. Single-feature methods include relying solely on curvature features, distance features, and local surface variation (LSV). Feature fusion is implemented using various clustering methods such as DBSCAN and K-means. Other types of methods encompass fast point feature histograms (FPFHs)[18], random sample consensus combined with DBSCAN (RANSAC-DBSCAN)[19], and least median of squares combined with principal component analysis (LMEDS-PCA)[20]. Furthermore, to ensure the stability and reliability of the metric data, repeated experiments were conducted and the average values were taken. These results were used to evaluate the performance of the algorithms.

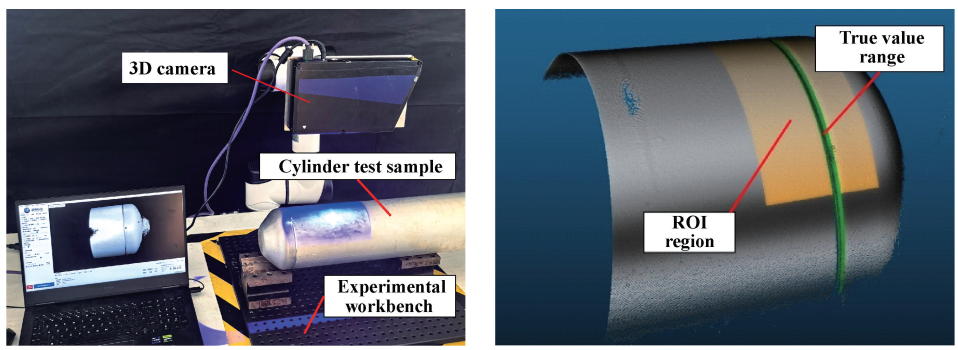


Fig. 8 Image acquisition and annotation of weld region

Figures 9(a)–9(i) visually demonstrate the weld region identification performance of different algorithms, with corresponding quantitative evaluation results summarized in Tables 1 and 2. Among single-feature methods, the single-feature curvature algorithm with a P of 90.65% is sensitive to noise, prone to misidentification and missed detection. The single-feature distance algorithm achieves a high R of 95.53% but a low P of only 78.92%, resulting in poor boundary recognition. The LSV algorithm exhibits obvious over-extraction, with a P of merely 72.85%, failing to meet high-precision identification requirements.

In comparisons using fused-features but different cluster strategies, fused-feature + DBSCAN achieves a P of 92.36%, an R of 94.97%, and an F_1 of 93.65%, which is close to the proposed algorithm. However, it is highly dependent on preset density parameters, with a V_{FP} value of 306, leading to noise misclustering. Due to its inherent spherical cluster assumption that is inconsistent with the actual weld morphology, fused-feature + K-means has an R of only 49.76%, suffering from severe missed identification and poor overall performance.

For other representative weld region identification algorithm, FPFH suffers from insufficient stability in smooth or noisy regions due to its reliance on local neighborhood calculations, resulting in highly fragmented segmentation outcomes, with an R of only 38.29%. RANSAC-DBSCAN achieves high precision and an F_1 of 91.94%, yet its DBSCAN component is still prone to noise misclassification caused by density irregularities, leading to false weld clusters. Meanwhile, LMEDS-PCA shows moderate precision (P = 84.33%) but exhibits inadequate discrimination capability in areas where the boundary between the base material and weld is indistinct, leading to excessive boundary extraction. In contrast, the proposed algorithm effectively addresses these limitations through multi-feature fusion. By leveraging the synergistic effects of GMM-based feature extraction and HDBSCAN, it achieves complete and robust weld region identification.

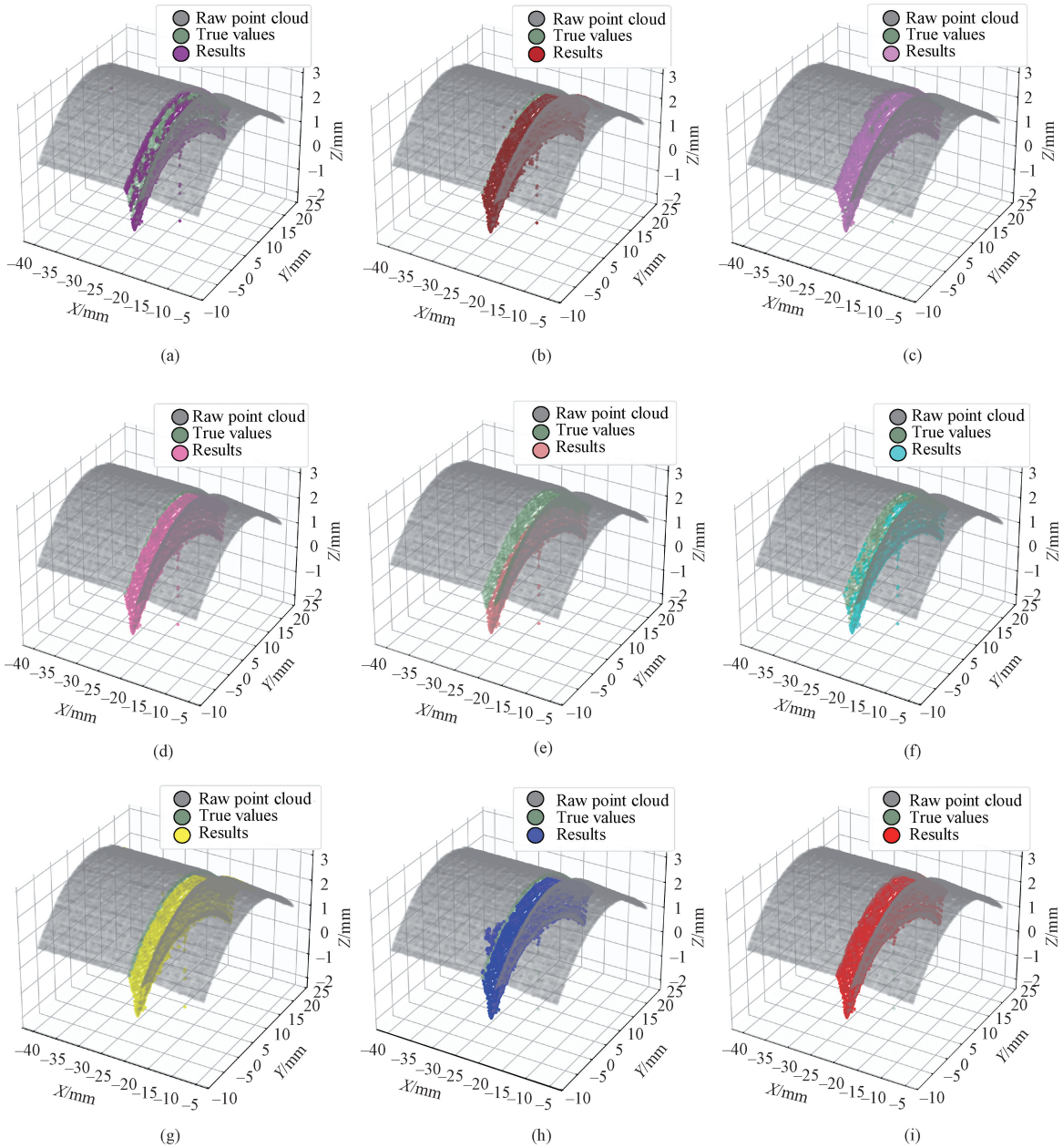


Fig. 9 Weld region identification results by different algorithms: (a) single-feature curvature; (b) single-feature distance; (c) LSV; (d) fused-feature +DBSCAN; (e) fused-feature + K-means; (f) FPFH; (g) RANSAC-DBSCAN; (h) LMEDS-PCA; (i) GMM-HDBSCAN

Table 1 Comparison of weld region identification results for different algorithms

Algorithm	Number of extraction points	V_{TP}	V_{FN}	V_{FP}
Single-feature curvature	2 652	2 404	1 472	248
Single-feature distance	4 721	3 726	174	995
LSV	4 605	3 355	522	1 250
Fused-feature + DBSCAN	4 006	3 700	196	306
Fused-feature + K-means	1 932	1 932	1 951	0
FPFH	1 522	1 483	2 390	39
RANSAC-DBSCAN	4 052	3 945	585	107
LMEDS-PCA	4 613	3 890	644	723
GMM-HDBSCAN	4 029	4 004	525	25

Table 2 Comparison of feature extraction performance for different algorithms

Algorithm	P/%	R/%	F_1/%	V_{RE}/%	Time/s
Single-feature curvature	90.65	62.02	73.65	37.98	0.93
Single-feature distance	78.92	95.53	86.43	4.46	0.12
LSV	72.85	86.53	79.11	13.46	1.71
Fused-feature + DBSCAN	92.36	94.97	93.65	5.03	0.09
Fused-feature + K-means	100.00	49.76	66.45	50.24	1.05
FPFH	97.44	38.29	54.98	61.71	15.33
RANSAC-DBSCAN	97.36	87.09	91.94	12.91	0.25
LMEDS-PCA	84.33	85.80	85.06	14.20	4.22
GMM-HDBSCAN	99.38	88.41	93.57	11.59	0.76

To validate the insensitivity to parameters of the proposed algorithm, we compare the parameter sensitivity of the two high-precision clustering methods, DBSCAN and HDBSCAN. The key parameters for DBSCAN are the neighborhood radius (eps) defining the search range during clustering and the minimum sample size (min_samples) specifying the minimum number of neighborhood points required for a core point. For HDBSCAN, the critical parameters are the minimum cluster size (min_cluster size) and min_samples. By adjusting various parameter settings, we recorded the parameter adjustment ranges and observed the variation in F_1. Additionally, a robustness index V_{RI} is introduced, defined as the percentage decrease in F_1 when parameters deviate by 10% from their optimal values. Table 3 shows that for DBSCAN, an absolute decrease of 8.2 percentage points in V_{RI} occurs when eps varies by 10% around its optimal value. Within the parameter range of 0.1–0.7, the absolute value of F_1 fluctuates by 26 percentage points. In contrast, HDBSCAN exhibits lower sensitivity, with an absolute decrease in V_{RI} by only 2.1 and 1.8 percentage points under parameter variations, and the absolute F_1 fluctuation remaining around 11 percentage points.

Table 3 Parameter sensitivity comparison of DBSCAN and HDBSCAN

Algorithm	Parameter	Parameter range	F_1/%	V_{RI}/%
DBSCAN	eps	0.1–0.7	64–90	8.2
	min_samples	3–25	76–89	3.5
HDBSCAN	min_cluster size	5–50	81–92	2.1
	min_samples	3–25	82–93	1.8

To quantify the boundary localization performance of the algorithm, we selected two comparison algorithms with the best overall performance: the fused-feature + DBSCAN algorithm and the RANSAC-DBSCAN algorithm. Boundary error analysis experiments were then conducted to compare their performance with that of the proposed GMM-HDBSCAN algorithm.

For the weld region boundaries extracted by the three algorithms and the manually annotated true boundaries, we randomly selected 400 boundary points from each dataset. Using the true boundary points as reference, we calculated the 3D Euclidean distance between the true and extracted boundary points. This distance value represents the localization error for a single boundary point. Subsequently, we plotted the indices of the 400 randomly selected boundary points on the x-axis to represent the random sampling positions, with the corresponding 3D Euclidean distances on the y-axis representing the single-point boundary errors, thereby generating a boundary error distribution curve.

As shown in Fig. 10, the curve corresponding to the proposed algorithm consistently lies at the bottom, indicating that the boundary error for most boundary points obtained by the proposed algorithm is lower than that by the fused-feature + DBSCAN and RANSAC-DBSCAN algorithms. The maximum boundary error of the proposed GMM-HDBSCAN algorithm is controlled within 0.3 mm. This further validates the effectiveness of the connected component analysis in the clustering stage and demonstrates the advantage of the proposed algorithm in boundary refinement. Additionally, the results confirm that the proposed algorithm achieves more stable and reliable boundary localization accuracy for weld region identification tasks in complex industrial environments.

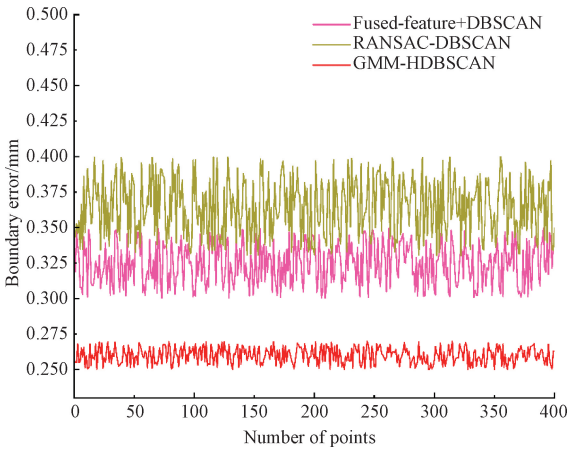


Fig. 10 Boundary error distribution

Beyond the comparison experiments described above, this paper also validates the effectiveness of the proposed algorithm in identifying weld regions on planar workpieces. As shown in Fig. 11, this method can identify weld regions across different types of welds on planar workpieces while effectively filtering noise interference. These results demonstrate that the proposed algorithm is not confined to circumferential welds. Its unsupervised learning framework, based on multi-feature fusion and an adaptive density clustering strategy, can effectively adapt to the geometric characteristics of welds with different structural types on planar workpieces. It is not constrained by workpiece surface morphology, weld type, or local feature variations, fully proving the strong generalizability of the algorithm in weld region identification tasks.

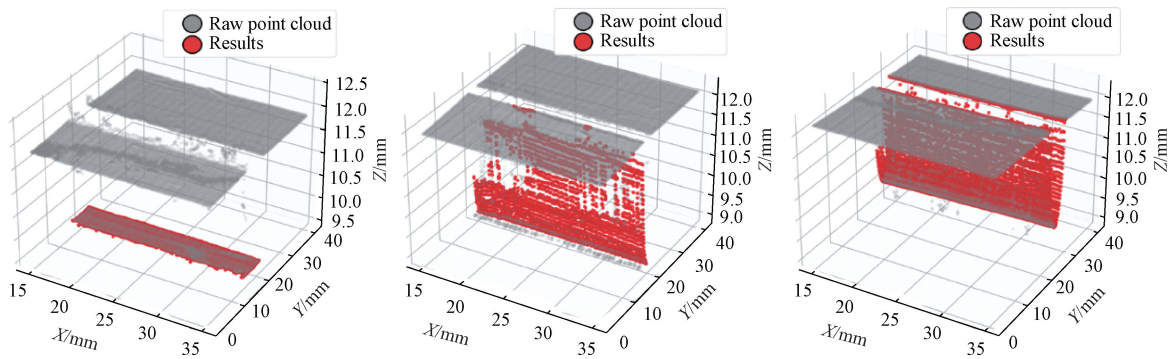


Fig. 11 Identification results for different weld types on planar workpieces: (a) straight weld; (b) V-groove weld; (c) U-groove weld

5 Conclusions

This study addresses the challenges in weld region identification caused by factors such as geometric complexity, assembly deviations, and point cloud noise, as well as the limitations of existing algorithms in terms of feature representation capability, parameter robustness, and boundary localization accuracy. An algorithm is proposed that integrates local geometric features and spatial distance features, employs a GMM for unsupervised modeling to extract feature points, and utilizes HDBSCAN density-adaptive clustering along with the connected component analysis to achieve precise identification of weld regions. Experimental results in real industrial scenarios demonstrate that the proposed GMM-HDBSCAN algorithm achieves a precision of 99.38% in weld region identification, with boundary localization errors controlled within 0.3 mm. Furthermore, parameter sensitivity experiments indicate that the algorithm exhibits low dependency on parameters such as the density threshold, showing good stability and adaptability under different working conditions. Extended experiments on various planar workpieces also verify the method's generalization capability for different weld types and geometric configurations. In summary, by effectively integrating local geometric and global spatial information, combined with adaptive density clustering and topology-constrained post-processing, the proposed algorithm achieves high-precision weld region identification. The results not only provide reliable guidance for automated welding systems but also establish a data foundation for subsequent weld quality assessment, dimensional inspection, and digital manufacturing processes.

References

[1] Liu Z Y, Hu J Q, Wang S, et al. Advance in quality control and in-service performance of laser welding for magnesium alloys in automotive applications [J]. *Rare Metal Materials and Engineering*, 2025, 54(5): 1377-1396. (in Chinese)

[2] Zhu D H, Wang S Z, Xu Z Y, et al. Research progress in robotic repair machining of complex component defects [J]. *Journal of Mechanical Engineering*, 2025, 61(11): 1-22. (in Chinese)

[3] He Y Y, Li Y, Xu Y. Segmentation of line laser strip on weld image under strong interferences

[J]. *Journal of Donghua University* (*English Edition*), 2026, 43(2): 120-127.
[4] Zhu M, Lei R J, Weng J, et al. MIG weld seam tracking system based on image automatic enhancement and attention mechanism deep learning[J]. *Transactions of the China Welding Institution*, 2024, 45(11): 90-94. (in Chinese)
[5] Jin H R, Sun Z R, Han X Y, et al. Assembly error analysis and control of thin-walled cylindrical parts in flight section of aircraft[J]. *Aeronautical Manufacturing Technology*, 2025, 68(18): 104-113, 132. (in Chinese)
[6] Wang Z. Review of real-time three-dimensional shape measurement techniques [J]. *Measurement*, 2020, 156: 107624.
[7] Malhan R K, Gupta S K. Planning algorithms for acquiring high fidelity pointclouds using a robot for accurate and fast 3D reconstruction [J]. *Robotics and Computer Integrated Manufacturing*, 2022, 78: 102372.
[8] Qian X M, Yang L J, Lou P H. Recognition of weld seam for pipe flange based on improved boundary following algorithm[J]. *Transactions of the China Welding Institution*, 2016, 37(12): 115-119, 134. (in Chinese)
[9] Ma W F, Wang J L, Zhang J P. Feature extraction from point cloud based on improved normal vector [J]. *Science of Surveying and Mapping*, 2021, 46(11): 84-90, 146. (in Chinese)
[10] Yang L, Liu Y H, Peng J Z, et al. A novel system for off-line 3D seam extraction and path planning based on point cloud segmentation for arc welding robot[J]. *Robotics and Computer-Integrated Manufacturing*, 2020, 64: 101929.
[11] Zhang Y K, Jiang Y, Tian X C, et al. A point cloud-based welding trajectory planning method for plane welds[J]. *The International Journal of Advanced Manufacturing Technology*, 2023, 125(3): 1645-1659.
[12] Gao J, Li F, Zhang C, et al. A method of D-type weld seam extraction based on point clouds[J]. *IEEE Access*, 2021, 9: 65401-65410.
[13] Zhang Y K, Geng Y S, Tian X C, et al. Feature extraction and robot path planning method in 3D vision-guided welding for multi-blade wheel structures[J]. *Optics and Lasers in Engineering*, 2024, 176: 108066.
[14] Zheng K, Xia X F, Qian J L, et al. Feature extraction of steel surface cracks based on point cloud multi-feature fusion [J]. *Laser Journal*, 2025, 46(8): 89-96. (in Chinese)
[15] Ke Y, Chen Y J, Zhang H, et al. Grinding track extraction of athletic shoes based on non-rigid point cloud registration[J]. *Journal of Donghua University* (*Natural Science*), 2023, 49(2): 92-98. (in Chinese)
[16] Yang L, Li E, Long T, et al. A novel 3-D path extraction method for arc welding robot based on stereo structured light sensor[J]. *IEEE Sensors Journal*, 2019, 19(2): 763-773.
[17] Yang B, Wang Z T, Xu Y T, et al. Surface segmentation and weld extraction on noisy point clouds consisting of multiple quadrics [J]. *Robotics and Computer-Integrated Manufacturing*, 2026, 97: 103100.
[18] Hegedus-Kuti J, Szolosi J, Varga M R T. 3D scanner-based identification of welding defects-clustering the results of point cloud alignment [J]. *Sensors*, 2023, 23(5): 2503.
[19] Zhou N, Jiang P, Jiang S L, et al. An identification and localization method for 3D workpiece welds based on the DBSCAN point cloud clustering algorithm [J]. *Journal of Manufacturing and Materials Processing*, 2024, 8(6): 287.
[20] Yang H T, Li X, Cheng Y L, et al. Adaptive segmentation method for weld seam point cloud based on normal features and LMedS [J]. *Modular Machine Tool & Automatic Manufacturing Technique*, 2025(3): 209-213, 218. (in Chinese)

基于特征融合的焊缝区域点云精准识别

马　达[1]，庞少儒[1]，王庆霞[1,3*]，吴重军[1]，董吉义[2,3]

1. 东华大学 机械工程学院，上海 201620
2. 上海航天设备制造总厂有限公司，上海 200245
3. 上海市航天工艺与装备工程技术研究中心，上海 200245

摘　要：为提升结构光视觉引导下焊缝区域识别的准确性并保持方法稳健，本文提出一种融合局部形态学特征与空间位置特征的自适应焊缝识别方法。首先，基于曲率估计和空间距离计算构建点云数据的二维特征空间，并采用高斯混合模型进行点云数据的无监督迭代学习，实现焊缝区域特征点提取。其次，结合层次密度聚类算法和体素连通块分析，完成焊缝区域的精确分割与边界细化。最后，实验结果表明，该方法对环形焊缝 V 型坡口区域进行识别时，精确率、召回率与 F1 分数分别达到 99.38%、88.41%和 93.57%，综合性能优于对比方法，如随机抽样一致性结合密度聚类算法。该方法的边界定位误差小于0.3 mm，且参数测试表明其参数敏感度低、稳定性强，能够满足实际生产应用需求。

关键词：结构光；点云数据；焊缝区域识别；高斯混合模型；层次密度聚类